Quantifying the effect of ICME removal and observation age for in situ solar wind data assimilation

Turner, H. ORCID: https://orcid.org/0000-0002-4012-8004, Owens, M. ORCID: https://orcid.org/0000-0003-2061-2453, Lang, M. ORCID: https://orcid.org/0000-0002-1904-3700, Gonzi, S. ORCID: https://orcid.org/0000-0002-0974-7392 and Riley, P. ORCID: https://orcid.org/0000-0002-1859-456X (2022) Quantifying the effect of ICME removal and observation age for in situ solar wind data assimilation. Space Weather, 20 (8). e2022SW003109. ISSN 1542-7390 doi: https://doi.org/10.1029/2022SW003109 Available at https://centaur.reading.ac.uk/106108/

www.reading.ac.uk/centaur

CentAUR

Central Archive at the University of Reading

Reading's research outputs online

Quantifying the Effect of ICME Removal and Observation Age for in Situ Solar Wind Data Assimilation

Harriet Turner[1] ⓘ, Mathew Owens[1] ⓘ, Matthew Lang[1] ⓘ, Siegfried Gonzi[2] ⓘ, and Pete Riley[3] ⓘ

[1]Department of Meteorology, University of Reading, Reading, UK, [2]Met Office, Exeter, UK, [3]Predictive Science Inc, San Diego, CA, USA

Abstract Accurate space weather forecasting requires advanced knowledge of the solar wind conditions in near-Earth space. Data assimilation (DA) combines model output and observations to find an optimum estimation of reality and has led to large advances in terrestrial weather forecasting. It is now being applied to space weather forecasting. Here, we use solar wind DA with in-situ observations to reconstruct solar wind speed in the ecliptic plane between 30 solar radii and Earth's orbit. This is used to provide solar wind speed hindcasts. Here, we assimilate observations from the Solar Terrestrial Relations Observatory and the near-Earth data set, OMNI. Analysis of two periods of time, one in solar minimum and one in solar maximum, reveals that assimilating observations from multiple spacecraft provides a more accurate forecast than using any one spacecraft individually. The age of the observations also has a significant impact on forecast error, whereby the mean absolute error (MAE) sharply increases by up to 23% when the forecast lead time first exceeds the corotation time associated with the longitudinal separation between the observing spacecraft and the forecast location. It was also found that removing coronal mass ejections from the DA input and verification time series reduces the forecast MAE by up to 10% as it removes false streams from the forecast time series. This work highlights the importance of an L5 space weather monitoring mission for near-Earth solar wind forecasting and suggests that an additional mission to L4 would further improve future solar wind DA forecasting capabilities.

Plain Language Summary The effects of space weather can be damaging to technologies on Earth, potentially causing power outages and posing a hazard to humans in space. Accurate space weather forecasting requires advanced knowledge of the solar wind; a continual outflow of material from the Sun. Data assimilation (DA) is one method used in terrestrial weather forecasting, whereby model results are combined with observations to create an optimum estimation of reality. Here, we use a solar wind DA scheme to create 3 years of forecasts. It is found that assimilating observations from multiple spacecraft produces better forecasts than assimilating observations from a single spacecraft. It was also found that removing large eruptions, known as coronal mass ejections, from the DA input improves forecasts by reducing false alarms.

1. Introduction

The changing plasma conditions in the near-Earth space environment is a major component of space weather (Lilensten & Belehaki, 2009). It poses a threat to modern life through damaging technology, causing power failures and posing a risk to the health of humans in space (Cannon, 2013). For accurate space weather forecasting, advanced knowledge of the solar wind conditions is required. The solar wind is a continual stream of charged particles that flows from the high temperature corona (Parker, 1958). The most severe space weather events occur as a result of coronal mass ejections (CMEs), large eruptions of coronal plasma and magnetic field (Webb & Howard, 2012). CMEs have to propagate through the ambient solar wind, so it acts to modulate the severity of the CME and its impacts on Earth (Cargill, 2004; Case et al., 2008). Stream interaction regions (SIRs) are an inherent feature of the ambient solar wind and are caused by fast streams catching up with slower streams and creating regions of higher plasma density and stronger magnetic field (Gosling & Pizzo, 1999; Richardson & Cane, 2012). SIRs which persist for more than one solar rotation, are also referred to as corotating interaction regions and provide a source of recurring space weather.

Solar wind forecasting can be achieved through simple empirical methods, such as corotation (Kohutova et al., 2016; Thomas et al., 2018; Turner et al., 2021) and persistence (Owens et al., 2013; Temmer et al., 2018), or through more complex, physics-based approaches such as magnetohydrodynamic (MHD) models (Merkin et al., 2016; Odstrcil, 2003; Riley et al., 2001; Tóth et al., 2005). We here focus on improving the latter.

Data assimilation (DA) combines prior information about a system (typically, from a numerical model) with observations to form an optimal estimation of reality, known as the posterior. It has been used extensively in terrestrial weather forecasting, leading to large improvements. It has been attempted in three major areas of space weather forecasting; the photosphere (e.g., Hickmann et al., 2015), the ionosphere (e.g., Elvidge & Angling, 2019) and the solar wind (e.g., Lang et al., 2017). Initial experiments in solar wind DA have shown potential for significant improvement in forecast skill (Lang et al., 2017). The BRaVDA (Burger Radius Variational Data Assimilation) methodology developed in Lang and Owens (2019) was subsequently used for producing hindcasts in Lang et al. (2021). BRaVDA uses a variational DA scheme (Dimet & Talagrand, 1986; Lorenc, 1986), with the simplified solar wind model, HUX (Riley & Lionello, 2011). The output from BRaVDA was used to initialize a second reduced-physics solar wind propagation model, HUXt (M. Owens et al., 2020), though it could equally be used with MHD models too. Lang et al. (2021) showed that whilst the 27-day forecast root mean square error was comparable to that of corotation forecasts, it showed improvement over non-DA forecasts. To further investigate the performance of the BRaVDA scheme and perform a more rigorous analysis, we have increased the hindcast cadence from 27-day to 1-day, as this is how forecasts would be generated if a DA scheme were deployed operationally.

The BRaVDA scheme makes use of in situ observations of near-Earth solar wind conditions from the OMNI data set (Vokhmyanin et al., 2019), and distant observations from the STEREO (Solar Terrestrial Relations Observatory) mission, which was launched in 2007 (Kaiser et al., 2008). The OMNI data set uses solar wind observations from a succession of spacecraft located at the L1 Lagrange point on the Sun-Earth line, at approximately 0.99AU. This is mostly comprised of observations from the *Wind* (Lepping et al., 1995; Ogilvie et al., 1993) and ACE (Advanced Composition Explorer; Stone et al., 1998) spacecraft propagated to the bow shock of Earth. The STEREO mission comprised of two spacecraft, STEREO-A and STEREO-B, which were placed into orbit around the Sun at approximately 1AU with STEREO-A ahead of Earth and STEREO-B behind. The spacecraft separate from Earth at approximately 22° per year and they passed behind the Sun in 2014. It was during this time that communication was lost with STEREO-B, and so the data used in this study is limited to STEREO-B's operational lifetime between 2007 and 2014.

The Lagrange points are gravitational nulls whereby the gravity of two large bodies balances the centripetal force of a smaller body. This means that spacecraft located at these positions will remain there, thus reducing the fuel required. There are five Lagrange points, with L4 and L5 positioned 60° ahead and behind Earth in its orbit, respectively. A spacecraft located at either point would provide a near side-on view of the Sun-Earth line and so could provide remote-sensing observations of Earth-directed CMEs. Extensive studies have also shown the potential usefulness of an in situ space weather monitor at L5 (e.g., Akioka et al. (2005); Simunac et al. (2009); Temmer et al. (2018)) and a mission is set for launch in 2027 (Davies, 2020). If this is joined by a space weather monitor at L4 (Posner et al., 2021), then these missions will provide additional observations that are useful for solar wind DA, as will be demonstrated in this study.

In this study, two analysis periods are used to assess the accuracy of hindcasts generated using the BRaVDA scheme. The methods used in this study are described in Section 2, with BRaVDA methodology described in Section 2.1 and the forecast generation method in Section 2.2. The data assimilation experiments and their results are described in Section 3. Finally, we discuss implications and draw conclusions in Section 4.

2. Methods

2.1. BRaVDA Scheme

The BRaVDA methodology was developed and extensively described in Lang and Owens (2019). The code is available at: https://github.com/University-of-Reading-Space-Science/BRaVDA. Here, we provide only a short overview of the methodology. BRaVDA is a variational DA scheme that incorporates in situ spacecraft observations of solar wind speed into the steady-state "HUX" solar wind model, based on Riley and Lionello (2011). Using the adjoint model of HUX, BRaVDA maps information contained within the in situ observations at 1 AU ($\sim$215 solar radii (R_S)) radially inwards to HUX's inner boundary at $30R_S$. This information is then merged with a prior inner-boundary condition through the minimization of a cost function comprised of the prior and observation errors weighted by their relative uncertainties. By finding the inner boundary condition that minimizes this cost function, we find the solar wind speeds with the lowest errors respective of their relative uncertainties.

This produces an updated inner boundary (the posterior state) which can be propagated radially outward by any solar wind model. For efficiency, we again use the HUX model, producing an optimal estimate of the true solar wind in the whole model domain, given the observations. The solar wind propagation model used in BRaVDA maps a 2 dimensional solar wind over the heliocentric domain from $30R_S$ to $236R_S$. The outer boundary here is an arbitrary choice, but it ensures that Earth's orbital radius is well within the boundary. We note that a different solar wind propagation model could be used to map the updated solar wind conditions out from $30R_S$ to Earth. For example,: Enlil (Odstrcil, 2003); HelioMAS (Riley et al., 2001); EUHFORIA (Pomoell & Poedts, 2018), or HUXt (Owens, 2020), could be used. As the solar wind is a highly driven system, we would expect similar improvements to the forecast skill from other solar wind models.

The BRaVDA scheme requires that we define our prior state (our current estimate of the inner boundary condition), the prior error covariance matrix (a measure of the uncertainty present in our prior information) and the observation error covariance matrix (that gives a measure of the uncertainty in our observations relative to the HUX model).

We generate our "prior" estimate of the solar wind speed at the inner boundary by using archived output of the HelioMAS model (data available from https://www.predsci.com/portal/home.php) at $30R_S$. HelioMAS is an MHD model that is initiated using radial magnetic field and solar wind speed derived from the coronal magnetic field topology (Riley et al., 2015) of the MAS (Magnetohydrodynamics Around a Sphere) model (Linker et al., 1999) solutions to the observed photospheric magnetic field. This prior state is then propagated out radially to $236R_S$ with the HUX model to generate a prior estimate of the solar wind speed at Earth.

The prior error covariance matrix is estimated from an ensemble of HUX initial conditions (see Lang et al. (2017) for more details) generated by perturbing the HelioMAS $30R_S$ solution in the same manner as Owens and Riley (2017). The observation error covariance contains not only the measurement error, but also representivity errors that arise from the incorrect specification of observations in numerical models (such as errors from assuming the observations are on the model gridpoints, sub-grid processes etc.). An example of such a representivity error in the BRaVDA scheme is the fact that the HUX model is 2-dimensional, meaning that observations are always assumed to be at the heliographic latitude of Earth, whereas in reality observations away from Earth (such as provided by STEREO) may be at other heliographic latitudes. This representivity error is a large unknown at present and an area of ongoing research (Lang et al. (2021); M. J. Owens et al. (2020); Turner et al. (2021)). In this study, we use the same observation error covariance matrix as in Lang et al. (2021) to maintain consistency with previous work.

In this study, BRaVDA is run for two time periods; 01/08/2009 to 01/02/2011 and 01/04/2012 to 01/10/2013. These periods are highlighted in Figure 3. The earlier period covers the 18-month up to the separation between solar minimum and the rise to solar maximum, as described in Turner et al. (2021), and the later period is around solar maximum. This allows for analysis of solar wind forecasts in both phases of the solar cycle.

BRaVDA is run at daily cadence, using in situ observations which would have been available at the time the forecast is performed, as in a genuine forecast. This expands on the work in Lang et al. (2021), where BRaVDA was run every 27 days. The prior state from HelioMAS, however, is only available as Carrington rotation solutions (i.e., every 27 days). In a true forecasting situation, the prior state would ideally be obtained from daily updated coronal solutions. However, the Carrington rotation solutions are adequate for our purposes here, as the DA process makes significant changes to the prior state. The likely effect of this is that the accuracy of the prior state is overestimated and the forecast improvement from DA reduced from the value expected in an operational situation.

The output from each BRaVDA run gives a 27-day solar wind reconstruction from $30R_S$ to $215R_S$, as shown in Figure 1. By taking the output from $215R_S$, this can be used as a solar wind time series for Earth and the STEREO spacecraft, as shown in Figure 2.

2.2. Forecast Generation

For each (daily) BRaVDA run, observations are assimilated from the previous 27 days up until the time the forecast is made, t_0. By assuming steady-state corotation of the posterior solution, each BRaVDA run can be used to generate a single forecast with a lead-time t_f of 0–27 days with respect to t_0. An example is shown in Figure 4.

CR2096
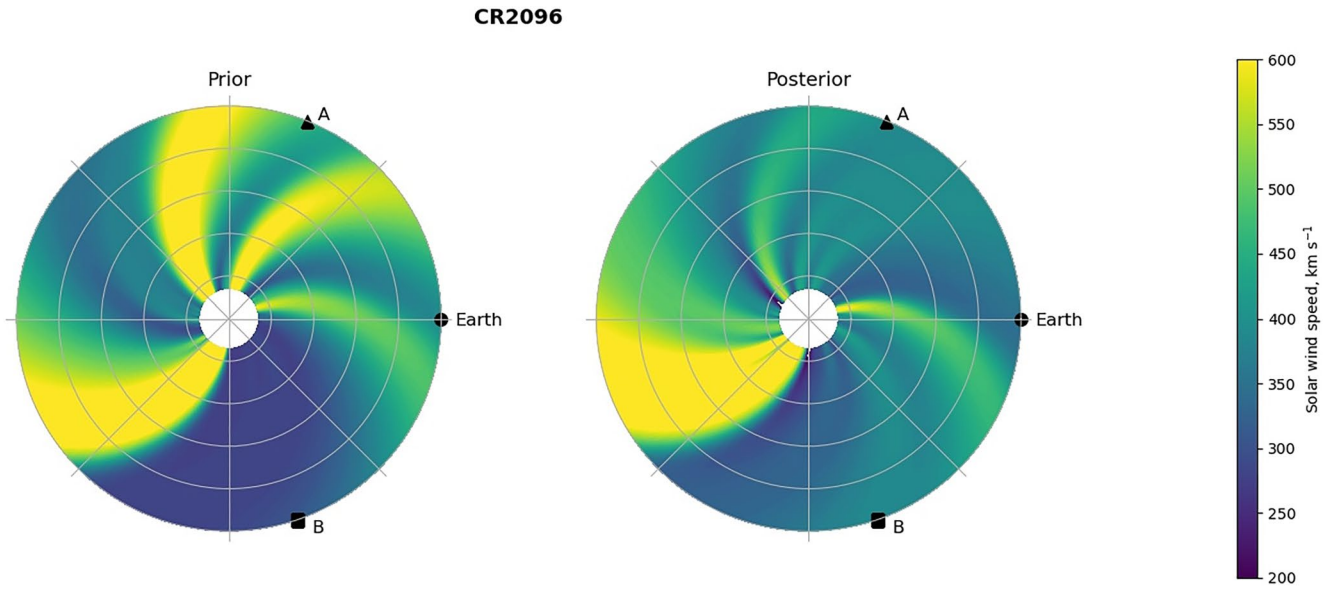
Figure 1. Solar wind solution from the HUX model initialized on 22/04/2010 for Carrington Rotation 2096 (22/04/2010 to 19/05/2010). The prior state (left) is that before the in situ data assimilation has taken place and the posterior state (right) is after the data assimilation. Indicated on both panels is the location of STEREO-A (A), Earth and STEREO-B (B) on 22/04/2010.

The single BRaVDA run produces a single solar wind speed estimate at each forecast lead time from 0 to 27 days. As BRaVDA is run on a daily cadence, a forecast time series for a particular lead time, for example, $t_f = 5$ days, at a given location can be created by combining forecasts for different t_0. While forecasts can be generated for the whole model domain, from $30R_S$ out to $215R_S$ and for all longitudes, here we only consider the locations of STEREO-A, STEREO-B and OMNI.
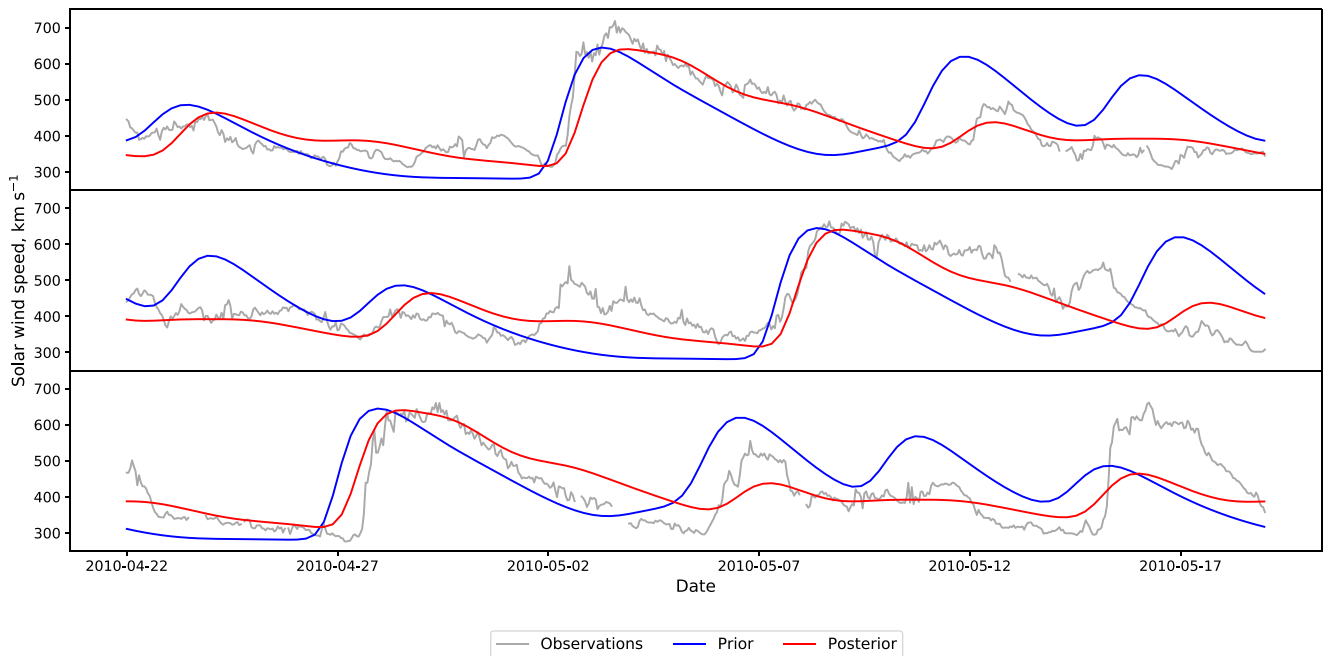
Figure 2. Time series at Earth's orbital distance of the solar wind solution for Carrington Rotation 2096 (22/04/2010 to 19/05/2010), as depicted in Figure 1. The top panel shows the solution at Earth, the middle panel at STEREO-A and the bottom panel at STEREO-B. The prior state is shown with the blue line, the posterior state with the red line and the gray line shows the observations taken from the respective spacecraft.
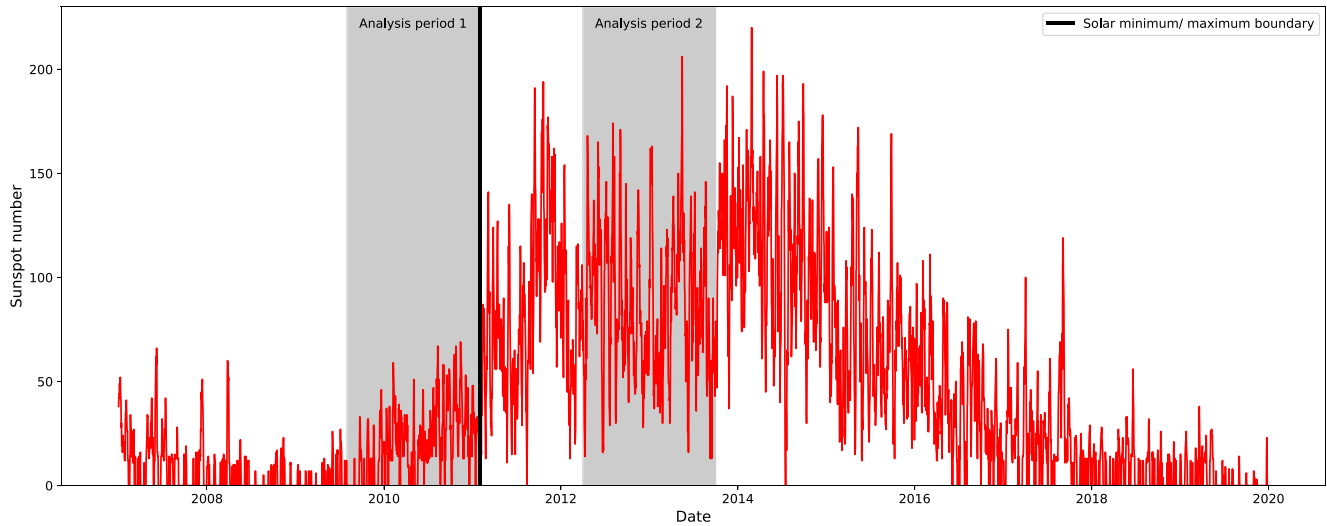
Figure 3. Evolution of sunspot number from 2007 to 2020. The analysis periods are highlighted in the gray shaded areas. The black vertical line shows the divide between solar minimum and solar maximum.

For the periods of time used in the analysis here, the spacecraft separation, and therefore corotation time between observation and Earth, changes over the analysis period (see Table 1).

3. Data Assimilation Experiments and Results

Throughout this study we consider the variation of forecast mean absolute error (MAE) with forecast lead time. Here we describe a number of individual BRaVDA experiments aimed at diagnosing specific aspects of forecast MAE.
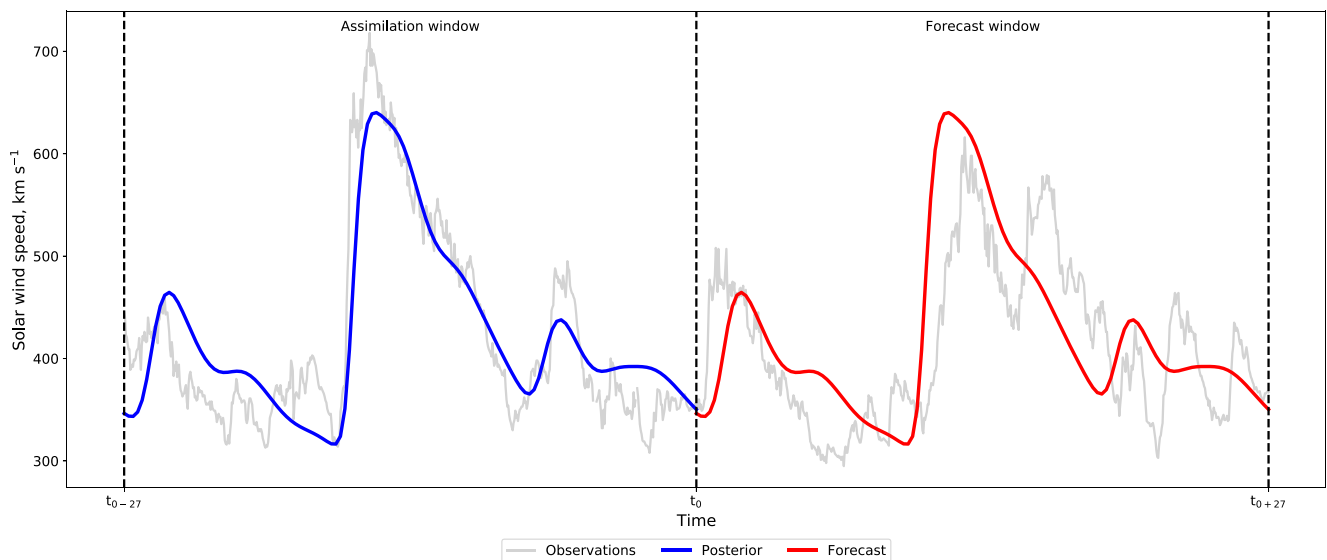
Figure 4. Using BRaVDA posterior output (blue) as a solar wind speed forecast (red). t_0 is the start of the forecast window, which here is 27 days long. It is also the end of the assimilation window, wherein observations from the previous 27 days up until t_0 are assimilated. The solar wind observations for this period are shown in gray.

Table 1
Corotation Time for the Different Spacecraft Pairings, Taking Into Account Only the Spacecraft Longitudinal Separation

Date	Spacecraft corotation time (days)					
	Earth to STA	STA to Earth	STB to Earth	Earth to STB	STB to STA	STA to STB
01/08/2009	4.3	22.7	3.7	23.3	8.0	18.9
01/02/2011	6.5	20.5	6.9	20.1	13.4	13.6
01/04/2012	8.3	18.7	8.9	18.1	17.2	9.8
01/10/2013	11.0	16.0	10.5	16.5	21.5	5.5

Note. The dates are the starts and ends of the solar minimum and solar maximum intervals.
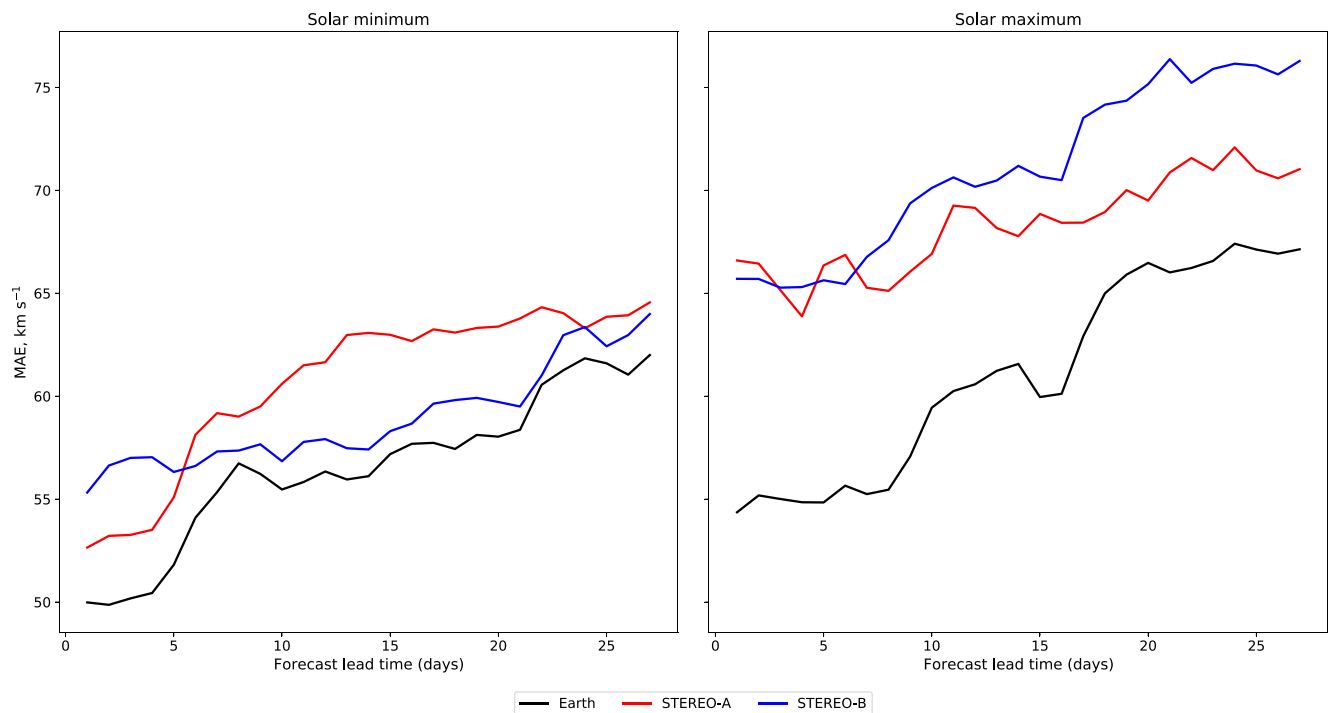
3.1. Forecast Lead Time

We first look at the effect of forecast lead time on MAE. For this, we assimilate observations from all three spacecraft (OMNI, STEREO-A and STEREO-B) and the output from BRaVDA is used to create forecasts at the locations of Earth, STEREO-A and STEREO-B for lead times of 0–27 days. This is done for both solar minimum and solar maximum time intervals. Figure 5 shows the MAE between the forecast and observed solar wind speed for a range of forecast lead times. As forecast lead time increases, there is a general trend for increasing forecast MAE. The left-hand panel shows the solar minimum interval, where MAE is generally lower than the solar maximum interval, shown in the right-hand panel. This is true for all three forecast locations. Note, however, that spacecraft separation (in solar longitude and latitude) also increases between these two time periods, so the difference in MAE between the solar minimum and maximum intervals cannot necessarily be attributed to the solar cycle. During the solar maximum interval, the MAE for the forecasts at the STEREO spacecraft is higher than for the forecasts at Earth. During this interval, the latitudinal separation between Earth and the STEREO spacecraft reaches a maximum of 14°, compared to 9° for the solar minimum interval (see Figure 1 in Turner et al., 2021). The difference between the forecast skill could be attributed to this greater latitudinal separation, combined with the generally more variable solar wind during solar maximum.

3.2. Assimilation of Individual Spacecraft and Age of Observations

We now consider the effect of assimilating different combinations of spacecraft. Experiments were carried out assimilating observations from all spacecraft together, as above, and assimilating the spacecraft observations individually. Figure 6 shows the MAE variation with forecast lead time for these different experiments. Here, the

Figure 5. Mean absolute error of solar wind forecasts as a function of forecast lead time, for the case where all spacecraft observations are assimilated. The forecast at Earth location is shown in black, at STEREO-A in red and at STEREO-B in blue. The solar minimum interval (01/08/2009 to 01/02/2011) is in the left-hand panel and the solar maximum interval (01/04/2012 to 01/10/2013) in the right-hand panel.
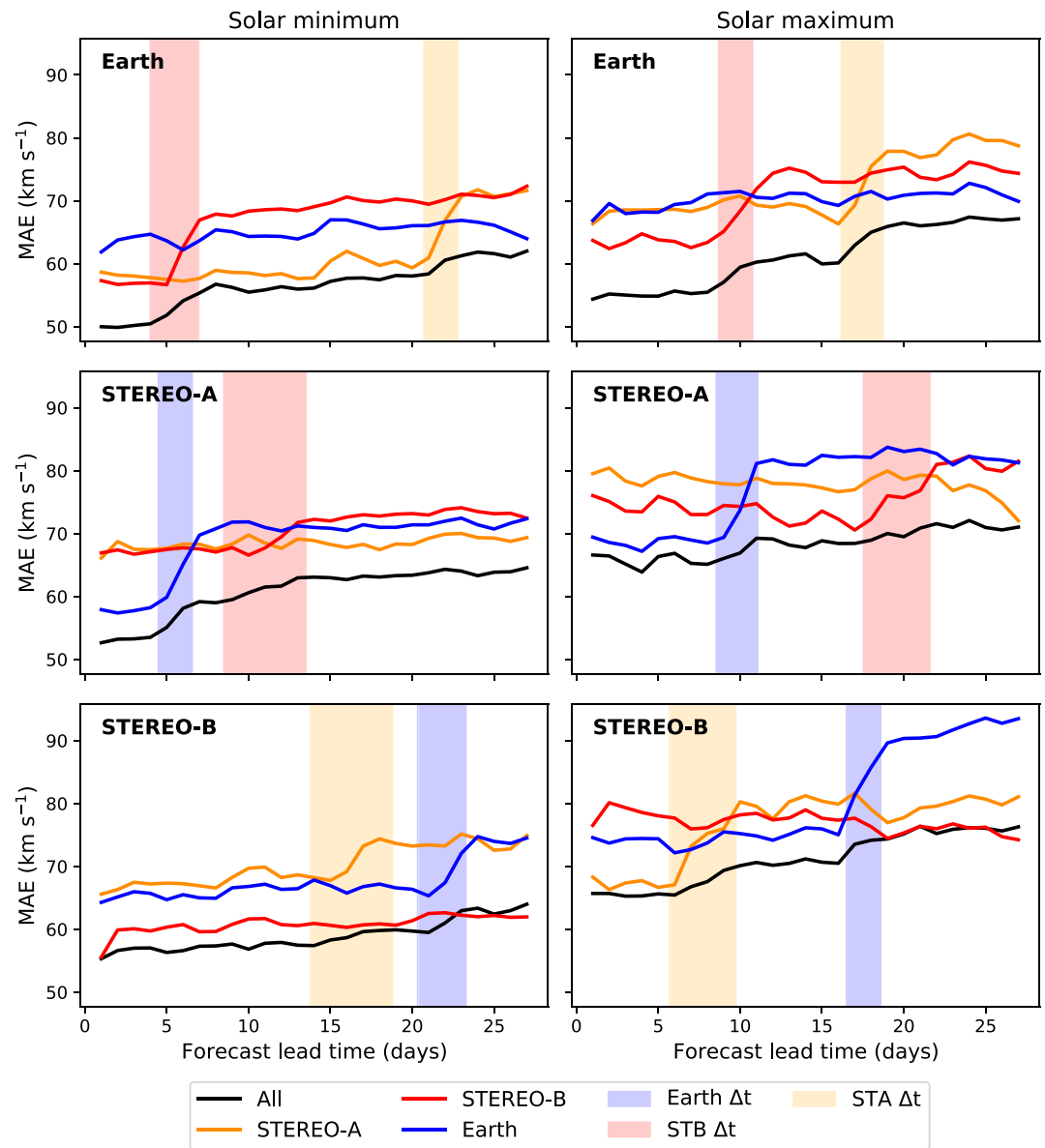
Figure 6. Mean absolute error of solar wind forecasts as a function of forecast lead time, for different combinations of assimilated spacecraft (colored lines, as indicated by the legend) and different forecast locations (rows of panels). The left hand column is the solar minimum interval, from 01/08/2009 to 01/02/2011, and the right hand column is the solar maximum interval, 01/04/2012 to 01/10/2013. The shaded regions show the corotation time from the spacecraft indicated by color (blue for Earth, yellow for STEREO-A and red for STEREO-B) to the forecast location.

forecasts at Earth location are in the top row, at STEREO-A in the second row and at STEREO-B in the bottom row. The solar minimum interval is in the left-hand column and solar maximum in the right-hand column.

The most obvious trend is that assimilating all spacecraft produces a forecast with the lower MAE than any one spacecraft individually. This is true at all locations and for all non-zero lead times. The exception is for very long lead-time forecasts (>20 days) at STEREO-B, where the MAE for assimilating all spacecraft is comparable to assimilating only STEREO-B data.

Overall, there is still a general trend of increasing MAE with lead time. When all spacecraft are assimilated, the MAE increase with lead time is fairly smooth, if not necessarily linear. When looking at the assimilation of individual spacecraft, however, there are clear step changes in MAE with forecast lead time. These can be understood in terms of the corotation time.

Forecast lead time at Earth	Days since the observation was at STEREO-B	Effective age of the observation
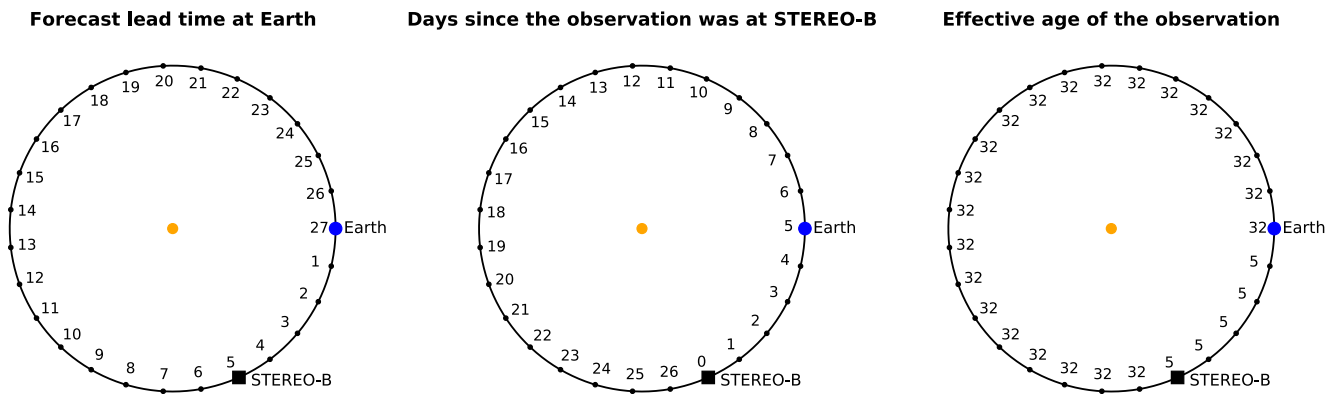
Figure 7. Schematics of the ecliptic plane to illustrate the effect of age of observations on solar wind data assimilation. The left-hand panel shows the time (in days) it takes the solar wind to corotate to Earth, which is the potential forecast lead time using observations from that location. The middle panel shows the number of days since solar wind at that position was last observed at STEREO-B. In this example, STEREO-B is approximately 65° behind Earth in Carrington longitude, as occurred in December 2009. The right-hand panel shows the effective age of STEREO-B observations for Earth forecasting, which is the sum of the forecast lead time and the number of days since the observation was observed.

When only individual spacecraft are assimilated, the lowest MAE at short, non-zero forecast lead times (e.g., <5 days) is obtained when assimilating the spacecraft "ahead" (in terms of solar rotation, meaning at lower Carrington longitude) of the forecast location. This can be seen in Figure 6; for example, the forecast MAE at STEREO-A's location (middle row) when assimilating only near-Earth observations (blue line) is initially below that obtained when assimilating only STEREO-A (orange line) or STEREO-B (red line). This remains the case for forecast lead times out to 5 days during the solar minimum period, and 10 days for the solar maximum period. Between these two time periods, STEREO-A separates from Earth, increasing from 57 to 87° ahead. Thus, observations at Earth provide recent information at STEREO-A for up to 5 and 10 days. The other panels show similar transitions are associated with the forecast lead time exceeding the corotation time. This effect can be seen schematically in Figure 7.

Table 2 shows the average MAE separated into intervals before and after when the lead time is less than or greater than the minimum corotation time between assimilated spacecraft and forecast location. For all assimilated spacecraft and forecast locations, there is an increase in MAE of between 8.5% and 23.2%, with an average value of 16.6%. Of course, increased lead time is expected to result in increased MAE, regardless of corotation time. But Figure 6 shows that this trend is much smaller, typically of the order a few percent.

The large jumps in MAE are due to the age of the observations, whereby once the forecast lead time (t_f) exceeds the corotation time (t_C), observations from the previous Carrington rotation are being used. This means that the effective age of observations (τ) for $t_f > t_C$ is $t_f + 27$ days. For example, when assimilating only STEREO-B and forecasting at Earth, as Table 1 shows, the corotation time increases from 3.7 to 6.9 days over the 01/08/2009 to 01/02/2011 period. Therefore, as lead times exceed ~5 days, we expect an increase in MAE as τ jumps from $\tau < 6.9$ to $\tau > 30.7$. This can be seen in Figure 6, where the red shaded region in the top left plot shows the corotation time for STEREO-B to Earth for that period. This effect can be seen in a number of other situations where single spacecraft are assimilated. When assimilating multiple spacecraft, the abrupt change in age of observation effect is lessened; although there is an increase in the forecast error over the shaded regions of Figure 6, the curve is not as steep as when assimilating only the spacecraft associated with that corotation time. Therefore, assimilating multiple spacecraft reduces the effect of the age of observations impacting the forecast MAE.

Figure 8 shows experiments where pairs of spacecraft observations are assimilated together (colored lines) for the different forecast locations compared

Table 2
Forecast Mean Absolute Error for Different Time Intervals, Different Locations and Different Assimilated Spacecraft

Assimilated spacecraft	Forecast location	MAE [km/s]					
		2009–2011			2012–2013		
		Before	After	% Diff	Before	After	% Diff
OMNI	Earth	-	-	-	-	-	-
	STEREO-A	57.8	71.2	23.2	68.7	82.0	19.4
	STEREO-B	66.1	74.5	12.7	74.5	91.7	23.1
STEREO-A	Earth	58.8	71.2	21.1	68.8	78.7	14.4
	STEREO-A	-	-	-	-	-	-
	STEREO-B	67.6	73.7	9.0	67.3	79.8	18.6
STEREO-B	Earth	57.0	69.6	22.1	63.4	74.2	17.0
	STEREO-A	67.3	73.0	8.5	73.6	81.1	10.2
	STEREO-B	-	-	-	-	-	-

Note. Before and After indicate forecasts where the lead time is less than or greater than the minimum corotation time between assimilated spacecraft and forecast location, respectively. Where it is left blank, this is because the lead time never exceeds the corotation time.
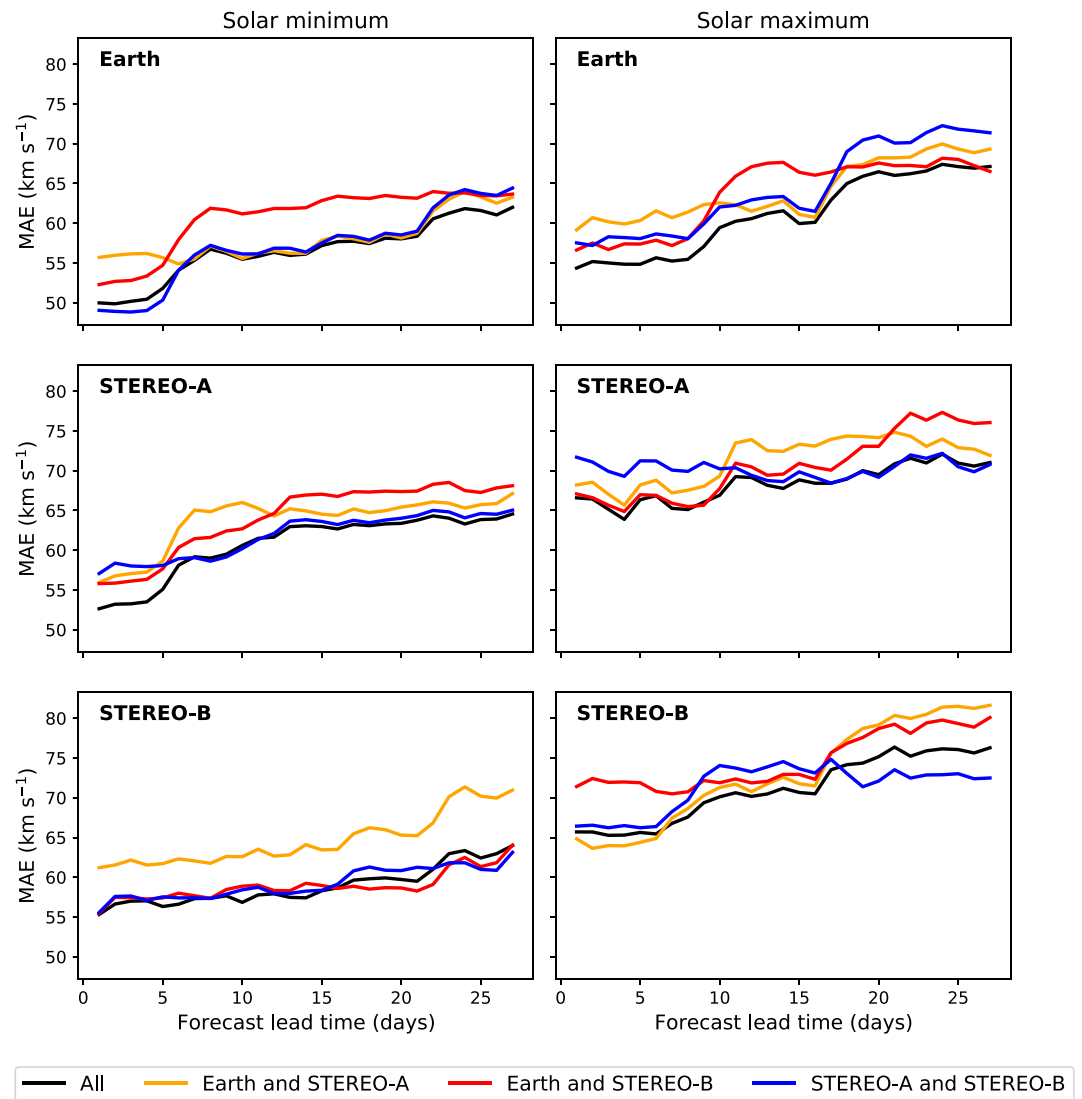
Figure 8. Mean absolute error of solar wind forecasts as a function of forecast lead time, for different pairs of assimilated spacecraft observations (colored lines, as indicated by the legend) and different forecast locations (rows of panels). The left hand column is the solar minimum interval, from 01/08/2009 to 01/02/2011, and the right hand column is the solar maximum interval, 01/04/2012 to 01/10/2013.

to when all three spacecraft observations are assimilated (black line). In general, it is preferable to assimilate all three observation sources than any two, though the difference is not as marked as that between three spacecraft and one, as shown in Figure 6. This is useful for future mission planning; for example, a pairing between the *Vigil* mission (ESA, 2022) and a near-Earth monitor. The jump in MAE due to the age of observations seen for single spacecraft in Figure 6 is reduced when including another observation source, but not completely removed. For example, the rise in MAE seen when assimilating only STEREO-B for a forecast at Earth (red line) in the top left panel in Figure 6 is still largely present when assimilating STEREO-B together with observations for near-Earth (red line) in the top left in Figure 8. Comparing that to when all three sources are assimilated (black line in top left in both Figures 6 and 8), that jump is less severe.

3.3. Removal of ICMEs

The interplanetary manifestations of CMEs (ICMEs) provide a potential source of error for forecasts using the DA output. For example, if a fast ICME encounters one of the assimilated spacecraft during the assimilation

window, the ICME will be reconstructed in the output as if it were a time-stationary fast solar wind stream. When this output is subsequently used for forecasting, it would produce a false fast stream in the forecast time series. Therefore, by removing ICMEs from the input time series of all spacecraft, the production of the false streams in the forecast time series can potentially be prevented.

Conversely, if a fast ICME encounters the forecast location during the forecast window, the forecast will miss the transient fast stream, as there will have been no corresponding fast stream in the assimilation window. Thus removing ICMEs from the verification time series allows us to better assess how well BRaVDA is reproducing the ambient solar wind structure, without penalizing for missing transient ICME structures, which it is not expected to capture. However, note that accurate reconstruction of the ambient solar wind is required to produce accurate ICME arrival time forecasts (e.g., Case et al., 2008). Thus we present results of removing ICMEs from the DA-input time series, the verification time series, and both. Times associated with ICMEs are identified using the HELCATS ICME list (Möstl et al., 2022). To ensure all of the disturbance associated with the ICME is removed, we eliminate 24 hr either side of the ICME leading disturbance and ICME trailing edge times. For the purposes of assimilated data, the data gap produced by removing an ICME is then linearly interpolated over to make a complete time series. Qualitatively similar results are obtained by simply removing times identified as ICMEs.

An example of the effect of removing ICMEs is shown in Figure 9. A fast ICME (maximum of 720 km s^{-1}) was identified at STEREO-B, seen as an isolated velocity spike between 22/09/2012 to 29/09/2012. This ICME was removed from the STEREO-B input and linearly interpolated to give the green line in the top panel of Figure 9. The bottom three panels show 5-day forecasts at Earth, STEREO-A and STEREO-B with (solid lines) and without (dashed lines) the ICME present in the assimilated STEREO-B time series. Red lines show assimilation of STEREO-B data only, while blues lines show assimilation of all three spacecraft data.

It can be seen that removing the ICME causes an improvement in the forecast, by removing a false fast stream, a certain time later. The time delay from ICME removal to forecast improvement relates to the corotation time between the spacecraft, which is determined by their longitudinal separation and can be seen in the gray shaded regions in Figure 9. At this time, the corotation time from STEREO-B to Earth is approximately 9 days, STEREO-B
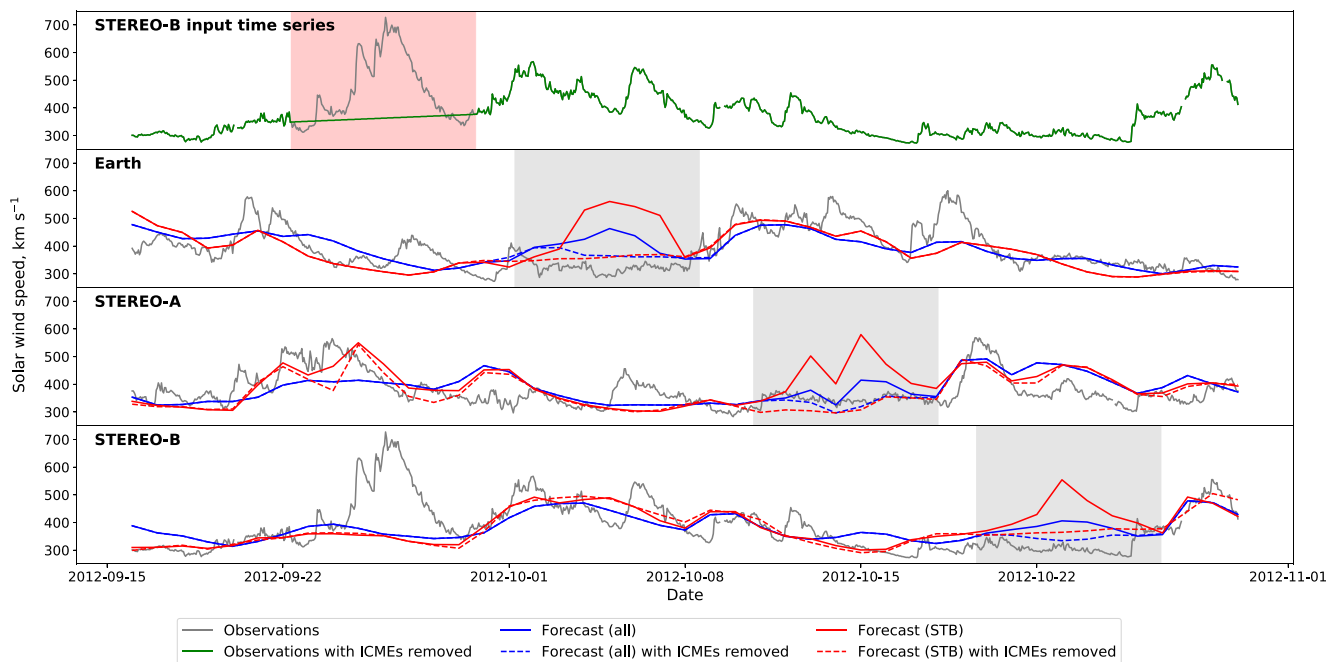
Figure 9. Time series of; top panel, the STEREO-B observations with the interplanetary manifestations of CME (ICME) included (gray) and with it removed (green); second panel, forecast with 5-day lead time for Earth; third panel, forecast with 5-day lead time for STEREO-A; bottom panel, forecast with 5-day lead time for STEREO-B. The blue lines show when all spacecraft observations are assimilated and the red lines show only STEREO-B observations assimilated. The solid line shows when the ICME is included in the STEREO-B input series and the dashed line when the ICME is removed. The red shaded region in the top panel shows the time span of the ICME plus 24 hr either side. The gray shaded regions in panels 2, 3 and 4 show the time span where the forecast time series has been influenced by the removal of the ICME.

to STEREO-A is approximately 18 days and the full Carrington rotation to STEREO-B is 27 days. It is after these respective times from the ICME that the improvement is seen in the forecast for that spacecraft. Furthermore, Figure 9 shows even without removal of ICMEs from the assimilation data (which may be difficult in real-time operational forecasting), assimilating multiple spacecraft observations reduces the magnitude of the false fast stream that is present in the forecasts following. Comparing the red and blue solid lines, when all spacecraft observations are assimilated, the false stream magnitude is reduced by approximately 150 km s^{-1} in the forecasts.

Figure 10 shows the variation of forecast MAE with forecast lead times for combinations of ICME removal from the DA input time series and the verification time series. There are four combinations; ICMEs remaining in both
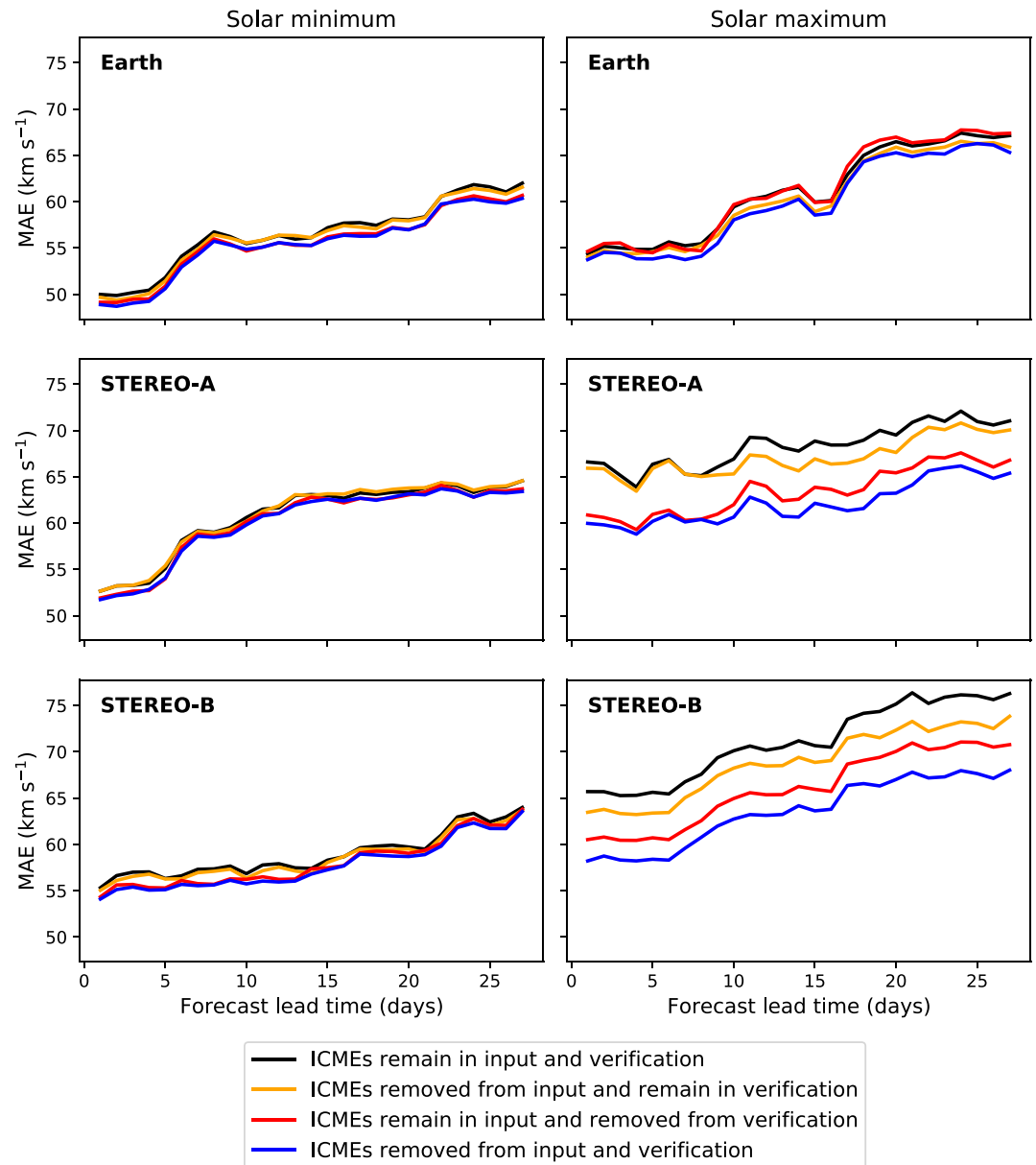
Figure 10. Variation of forecast mean absolute error with forecast lead time for different combinations of interplanetary manifestations of CME (ICME) removal from the input and verification time series. The black line shows the case when the ICMEs remain in both data assimilation (DA) input and verification time series. The red line shows the case when ICMEs are removed from the verification time series only. The orange line shows the case when ICMEs are removed from the DA input series only. The blue line shows the case when ICMEs are removed from both the DA input and verification time series. All spacecraft are assimilated in all cases.

Table 3

Average Forecast Mean Absolute Error (Over All Lead Times) for Combinations of Removing Interplanetary Manifestations of CMEs (ICMEs) From the Data Assimilation Input Time Series and the Verification Time Series

ICMEs in input?	ICMEs in verification?	Solar minimum			Solar maximum		
		Earth	STA	STB	Earth	STA	STB
Yes	Yes	56.1	60.3	58.7	60.7	68.1	70.7
	No	55.2	59.8	57.8	60.8	63.1	65.6
No	Yes	55.9	60.4	58.4	60.0	66.9	68.4
	No	55.1	59.6	57.5	59.5	61.9	63.1

Note. The average MAE is shown for both the solar minimum (01/08/2009 to 01/02/2011) and solar maximum (01/04/2012 to 01/10/2013) intervals. Top row: ICMEs are included in both the DA input and verification time series. Second row: ICMEs are included in the DA input time series and removed from the verification time series. Third row: ICMEs are removed from the DA input time series and remain in the verification time series. Bottom row: ICMEs are removed from both the DA input and verification time series.

time series, ICMEs removed from the input time series but remaining in the verification time series, ICMEs remaining in the input time series but removed from the verification time series and ICMEs removed from both time series. It can be seen from Figure 10 and from the average MAE values in Table 3 that, generally, removing ICMEs leads to forecast improvement. For example, for the forecast at Earth, the average MAE across all lead times is 56.1 and 60.7 km s^{-1} for the solar minimum and solar maximum intervals respectively. By removing ICMEs from both the input and verification time series, these are reduced to 55.1 km s^{-1} for solar minimum and 59.5 km s^{-1} for solar maximum, which is a percentage difference of −1.8% and −2.0% respectively, as shown in Table 4. There is greater improvement in the solar maximum period, particularly at STEREO-A and STEREO-B. This is due to a larger number of ICMEs at this time, with a total number of 72 ICMEs observed during the solar minimum period compared to 138 during the solar maximum period. We further classify fast ICMEs as those with an average proton speed of more than 500 km s^{-1}, as taken from the HELCATS ICME catalog. 20 fast ICMEs were observed during the solar maximum period and 6 during the solar minimum period. Out of the 20 fast ICMEs during the solar maximum period, five of these were at Earth, 7 at STEREO-A and 8 at STEREO-B. Although only a small difference between the spacecraft, this could account for the −2.0% difference at Earth compared with the −9.1% at STEREO-A and −10.7% at STEREO-B. On average, we would not expect such a large difference between the forecasts at the STEREO spacecraft and at Earth. However, here we have a small sample size and so the properties of the individual ICMEs have a greater impact.

4. Discussion and Conclusions

In this study we have performed a number of solar wind data assimilation experiments to determine how forecast error is expected to vary with a number of different factors. Here, MAE was used as the metric to analyze the forecast accuracy. Although MAE is a single metric and it can sometimes mislead (Owens, 2018), it is useful here as the individual changes to the DA process that we are testing produce time series that are, for the most part, qualitatively similar. Future work will focus on a more complete analysis of forecast performance.

We have shown that assimilating observations from multiple spacecraft produces a forecast with lower MAE than when assimilating observations from any one single spacecraft. This is despite the fact that observations may not be ideally placed, due to the inclination of the ecliptic plane to the solar equator (Owens et al., 2019; M. J. Owens et al., 2020). Assimilating two sources of well separated observations is preferable to one source, and three sources is preferable to two. However, the difference between one and two sources of observations is greater than two and three. Assimilation of the STEREO spacecraft observations, along with OMNI, has shown to improve forecasts and so the addition of space weather monitors at both L4 and L5 can only aid future development of solar wind DA. This stresses the value of multiple, well separated, space weather monitoring missions, such as at the L5 point (Lagrange mission, Davies, 2020), but also the importance of a mission to the L4 point (see Posner et al., 2021).

Table 4

Percentage Difference of the Average Mean Absolute Error for Forecasts (Over All Lead Times) With Combinations of Interplanetary Manifestations of CMEs (ICMEs) Removed From the Data Assimilation Input Time Series and Verification Time Series Compared With the Forecasts Where ICMEs Remain

ICMEs in input?	ICMEs in verification?	Solar minimum			Solar maximum		
		Earth	STA	STB	Earth	STA	STB
Yes	No	−1.6	−0.8	−1.5	0.2	−7.3	−7.2
No	Yes	−0.4	0.2	−0.5	−1.2	−1.8	−3.3
	No	−1.8	−1.2	−2.0	−2.0	−9.1	−10.7

Note. Where the difference is negative, this indicates the average MAE without ICMEs is smaller than with ICMEs included. Top row: ICMEs remain in the DA input time series and are removed from the verification time series. Middle row: ICMEs are removed from the DA time series and remain in the verification time series. Bottom row: ICMEs are removed from both the DA input and verification time series.

The "age" of the observations, in terms of the time since a Carrington longitude was last observed by a particular spacecraft, also has a large effect on forecast error. When assimilating data from a single spacecraft, there is a large increase in MAE once the forecast lead time is greater than the corotation time from that spacecraft to the forecast location. This is due to the assumption of steady state conditions becoming increasingly less valid. Although assimilating multiple spacecraft does not completely remove this

effect, it is greatly reduced and the discontinuous increases in MAE with forecast lead time are reduced. But further forecast improvement may be obtained by weighting observations by their age. Simple experiments testing this idea with BRaVDA (not shown) have been inconclusive. However, as BRaVDA is based upon HUX (Riley & Lionello, 2011), which is not time dependent, it is not easy to explicitly implement this. Future experiments using the time-dependent version of HUX (HUXt, M. Owens et al., 2020) are planned.

ICMEs have the potential to introduce false streams into the BRaVDA output, leading to false alarms in the forecasts. As ICMEs are transient events rather than corotating solar wind streams, they are not correctly captured in BRaVDA. If a fast ICME encounters one of the assimilating spacecraft, it will be treated as a fast ambient solar wind stream and assumed to persist at the observed Carrington longitude. Thus a fast stream is subsequently incorrectly forecast. This was demonstrated when considering a single fast ICME encountered by STEREO-B in late September 2012. This ICME was removed from the input observations at STEREO-B and the resulting BRaVDA output was used for forecasting at Earth, STEREO-A and STEREO-B. There was a marked improvement in the 5-day lead time forecast time series at Earth, STEREO-A and STEREO-B, through reduction of a region of forecast high solar wind. This was seen for the cases where only STEREO-B observations were assimilated and when all three spacecraft observations were assimilated. When only the STEREO-B observations were assimilated, the false fast stream appeared larger in the forecast time series than when all spacecraft observations were assimilated, as the ICME was only observed at one spacecraft. Although assimilation of multiple observations caused this false alarm to be of a lower magnitude than the fast ICME in the observations, it did not completely remove it.

More generally, applying the ICME removal to the solar minimum and solar maximum time periods showed a general improvement in the forecast accuracy. However, improvements were modest, as all three spacecraft were assimilated, which already reduces the effect of transient ICMEs.

The largest improvement was in the solar maximum period at STEREO-A and STEREO-B, due to the larger number of fast ICMEs observed at these spacecraft. It was found that removing ICMEs from the verification time series caused a larger improvement in the forecast MAE than removing them from the DA input time series. This is due to BRaVDA missing fast streams having a larger effect than creating fast streams through misinterpreting an ICME. As an ICME would be observed at only one spacecraft, assimilating multiple observations limits the reconstruction of the ICME as a steady-state solar wind structure, thus reducing the production of a false alarm in the forecast. For BRaVDA to be deployed operationally, an algorithm to automatically detect and remove ICMEs from the real time solar wind data would be required. Some methods based on proton temperature (Cane & Richardson, 2003) and iron charge state have been tested with corotation forecasts (Kohutova et al., 2016). Removing ICMEs using these indicators led to an improvement in forecast skill score, so this technique could be applied for operational DA. Developing BRaVDA for operational solar wind forecasting will additionally require the use of real-time spacecraft observations, analysis of which is left for future work.

Data Availability Statement

OMNI data were downloaded from the OMNIWeb portal at https://omniweb.gsfc.nasa.gov/ow.html. STEREO-A and STEREO-B data were downloaded from the CDAWeb Data Explorer portal at https://cdaweb.gsfc.nasa.gov/. Spacecraft location data were downloaded from https://omniweb.gsfc.nasa.gov/coho/helios/heli.html. HelioMAS model output is available from the Predictive Science Inc (website: http://www.predsci.com/mhdweb/home.php).

References

Akioka, M., Nagatsuma, T., Miyake, W., Ohtaka, K., & Marubashi, K. (2005). The L5 mission for space weather forecasting. *Advances in Space Research*, *35*(1), 65–69. https://doi.org/10.1016/j.asr.2004.09.014

Cane, H. V., & Richardson, I. G. (2003). Interplanetary coronal mass ejections in the near-Earth solar wind during 1996-2002. *Journal of Geophysical Research*, *108*(A4), 1156. https://doi.org/10.1029/2002JA009817

Cannon, P. S. (2013). Extreme space weather - A report published by the UK royal academy of engineering. *Space Weather*, *11*(4), 138–139. https://doi.org/10.1002/swe.20032

Cargill, P. J. (2004). On the aerodynamic drag force acting on interplanetary coronal mass ejections. *Solar Physics*, *221*(1), 135–149. https://doi.org/10.1023/B:SOLA.0000033366.10725.a2

Case, A. W., Spence, H. E., Owens, M. J., Riley, P., & Odstrcil, D. (2008). Ambient solar winds' effect on ICME transit times. *Geophysical Research Letters*, *35*(15), 1–5. https://doi.org/10.1029/2008GL034493

Davies, J. (2020). The COR and HI instruments for the Lagrange L5 mission. In *The cor and hi instruments for the Lagrange l5 mission*.

Dimet, F. L., & Talagrand, O. (1986). Variational algorithms for analysis and assimilation of meteorological observations: Theoretical aspects. *Tellus*, *38A*(2), 97–110. https://doi.org/10.1111/j.1600-0870.1986.tb00459.x

Elvidge, S., & Angling, M. J. (2019). Using the local ensemble Transform Kalman Filter for upper atmospheric modelling. *Journal of Space Weather and Space Climate*, *9*, A30. https://doi.org/10.1051/swsc/2019018

ESA. (2022). Introducing ESA Vigil: Earth's devoted solar defender. Retrieved from https://www.esa.int/Safety{_}Security/Space{_}weather/Introducing{_}ESA{_}Vigil{_}Earth{_}s{_}devoted{_}solar{_}defender

Gosling, J. T., & Pizzo, V. J. (1999). Formation and evolution of corotating interaction regions and their three dimensional structure. *Space Science Reviews*, *89*, 21–52. https://doi.org/10.1007/978-94-017-1179-1_3

Hickmann, K. S., Godinez, H. C., Henney, C. J., & Arge, C. N. (2015). Data assimilation in the ADAPT photospheric flux transport model. *Solar Physics*, *290*(4), 1105–1118. https://doi.org/10.1007/s11207-015-0666-3

Kaiser, M. L., Kucera, T. A., Davila, J. M., Cyr, O. C., Guhathakurta, M., & Christian, E. (2008). The STEREO mission: An introduction. *Space Science Reviews*, *136*(1–4), 5–16. https://doi.org/10.1007/s11214-007-9277-0

Kohutova, P., Bocquet, F. X., Henley, E. M., & Owens, M. J. (2016). Improving solar wind persistence forecasts: Removing transient space weather events, and using observations away from the Sun-Earth line. *Space Weather*, *14*(10), 802–818. https://doi.org/10.1002/2016SW001447

Lang, M., Browne, P., van Leeuwen, P. J., & Owens, M. (2017). Data assimilation in the solar wind: Challenges and first results. *Space Weather*, *15*(11), 1490–1510. https://doi.org/10.1002/2017SW001681

Lang, M., & Owens, M. J. (2019). A variational approach to data assimilation in the solar wind. *Space Weather*, *17*(1), 59–83. https://doi.org/10.1029/2018SW001857

Lang, M., Witherington, J., Owens, M. J., Turner, H., & Riley, P. (2021). Improving solar wind forecasting using Data Assimilation. *Space Weather*, *19*(7), e2020SW002698. https://doi.org/10.1029/2020sw002698

Lepping, R. P., Acũna, M. H., Burlaga, L. F., Farrell, W. M., Slavin, J. A., Schatten, K. H., et al. (1995). The WIND magnetic field investigation. *Space Science Reviews*, *71*(1–4), 207–229. https://doi.org/10.1007/BF00751330

Lilensten, J., & Belehaki, A. (2009). Developing the scientific basis for monitoring, modelling and predicting space weather. *Acta Geophysica*, *57*(1), 1–14. https://doi.org/10.2478/s11600-008-0081-3

Linker, J. A., Mikić, Z., Biesecker, D. A., Forsyth, R. J., Gibson, S. E., Lazarus, A. J., et al. (1999). Magnetohydrodynamic modeling of the solar corona during whole Sun month. *Journal of Geophysical Research*, *104*(A5), 9809–9830. https://doi.org/10.1029/1998JA900159

Lorenc, A. C. (1986). Analysis methods for numerical weather prediction. *Quarterly Journal of the Royal Meteorological Society*, *112*(474), 1177–1194. https://doi.org/10.1002/qj.49711247414

Merkin, V. G., Lyon, J. G., Lario, D., Arge, C. N., & Henney, C. J. (2016). Time-dependent magnetohydrodynamic simulations of the inner heliosphere. *Journal of Geophysical Research - A: Space Physics*, *121*(4), 2866–2890. https://doi.org/10.1002/2015JA022200

Möstl, C., Boakes, P., Isavnin, A., Kilpua, E. K., Winslow, R., Anderson, B., et al. (2022). HELCATS WP4 catalogue. Retrieved from https://www.helcats-fp7.eu/catalogues/wp4{_}icmecat.html.%2010.6084/m9.figshare.4588315.v1

Odstrcil, D. (2003). Modeling 3-D solar wind structure. *Advances in Space Research*, *32*(4), 497–506. https://doi.org/10.1016/S0273-1177(03)00332-6

Ogilvie, K. W., Chornay, D. J., Fritzenreiter, R. J., Hunsaker, F., Keller, J., Lobell, J., et al. (1993). Swe, a comprehensive plasma instrument for the wind spacecraft. *Space Science Reviews*, *8*(71), 55–77. https://doi.org/10.1007/bf00751326

Owens, M. (2020). Solar-wind structure (No. July). https://doi.org/10.1093/acrefore/9780190871994.013.19

Owens, M., Lang, M., Barnard, L., Riley, P., Ben-Nun, M., Scott, C. J., et al. (2020). A computationally efficient, time-dependent model of the solar wind for use as a surrogate to three-dimensional numerical magnetohydrodynamic simulations. *Solar Physics*, *295*(3), 43. https://doi.org/10.1007/s11207-020-01605-3

Owens, M. J. (2018). Time-window approaches to space-weather forecast metrics: A solar wind case study. *Space Weather*, *16*(11), 1847–1861. https://doi.org/10.1029/2018SW002059

Owens, M. J., Challen, R., Methven, J., Henley, E., & Jackson, D. R. (2013). A 27 day persistence model of near-Earth solar wind conditions: A long lead-time forecast and a benchmark for dynamical models. *Space Weather*, *11*(5), 225–236. https://doi.org/10.1002/swe.20040

Owens, M. J., Lang, M., Riley, P., Lockwood, M., & Lawless, A. S. (2020). Quantifying the latitudinal representivity of in situ solar wind observations. *Journal of Space Weather and Space Climate*, *10*, 8. https://doi.org/10.1051/swsc/2020009

Owens, M. J., & Riley, P. (2017). Probabilistic solar wind forecasting using large ensembles of near-sun conditions with a simple one-dimensional "upwind" scheme. *Space Weather*, *15*(11), 1461–1474. https://doi.org/10.1002/2017SW001679

Owens, M. J., Riley, P., Lang, M., & Lockwood, M. (2019). Near-Earth solar wind forecasting using corotation from L5: The error introduced by heliographic latitude offset. *Space Weather*, *17*(7), 1105–1113. https://doi.org/10.1029/2019SW002204

Parker, E. N. (1958). Dynamics of the interplanetary gas and magnetic fields. *The Astrophysical Journal*, *128*, 664. https://doi.org/10.1086/146579

Pomoell, J., & Poedts, S. (2018). Euhforia: European heliospheric forecasting information asset. *Journal of Space Weather and Space Climate*, *8*, A35. https://doi.org/10.1051/swsc/2018020

Posner, A., Arge, C. N., Staub, J., StCyr, O. C., Folta, D., Solanki, S. K., et al. (2021). A multi-purpose heliophysics L4 mission. *Space Weather*, *19*(9), 1–27. https://doi.org/10.1029/2021SW002777

Richardson, I. G., & Cane, H. V. (2012). Solar wind drivers of geomagnetic storms during more than four solar cycles. *Journal of Space Weather and Space Climate*, *2*, 1–9. https://doi.org/10.1051/swsc/2012001

Riley, P., Linker, J. A., & Arge, C. N. (2015). On the role played by magnetic expansion factor in the prediction of solar wind speed. *Space Weather*, *13*(3), 154–169. https://doi.org/10.1002/2014SW001144

Riley, P., Linker, J. A., & Mikić, Z. (2001). An empirically-driven global MHD model of the solar corona and inner heliosphere. *Journal of Geophysical Research*, *106*(A8), 15889–15901. https://doi.org/10.1029/2000ja000121

Riley, P., & Lionello, R. (2011). Mapping solar wind streams from the Sun to 1 AU: A comparison of techniques. *Solar Physics*, *270*(2), 575–592. https://doi.org/10.1007/s11207-011-9766-x

Simunac, K. D. C., Kistler, L. M., Galvin, A. B., Popecki, M. A., & Farrugia, C. J. (2009). In situ observations from STEREO/PLASTIC: A test for L5 space weather monitors. *Annales Geophysicae*, *27*(10), 3805–3809. https://doi.org/10.5194/angeo-27-3805-2009

Stone, E. C., Frandsen, A. M., Mewaldt, R. A., Christian, E., Margolies, D., Ormes, J., & Snow, F. (1998). The advanced composition explorer. *Space Science Reviews*, *86*(1–4), 1–22. https://doi.org/10.1023/A:1005082526237

Temmer, M., Hinterreiter, J., & Reiss, M. A. (2018). Coronal hole evolution from multi-viewpoint data as input for a STEREO solar wind speed persistence model. *Journal of Space Weather and Space Climate*, *8*, A18. https://doi.org/10.1051/swsc/2018007

Thomas, S. R., Fazakerley, A., Wicks, R. T., & Green, L. (2018). Evaluating the skill of forecasts of the near-Earth solar wind using a space weather monitor at L5. *Space Weather*, *16*(7), 814–828. https://doi.org/10.1029/2018SW001821

Tóth, G., Sokolov, I. V., Gombosi, T. I., Chesney, D. R., Clauer, C. R., De Zeeuw, D. L., et al. (2005). Space weather modeling framework: A new tool for the space science community. *Journal of Geophysical Research*, *110*(A12), 1–21. https://doi.org/10.1029/2005JA011126

Turner, H., Owens, M. J., Lang, M. S., & Gonzi, S. (2021). The influence of spacecraft latitudinal offset on the accuracy of corotation forecasts. *Space Weather*, *19*(8), 1–15. https://doi.org/10.1029/2021sw002802

Vokhmyanin, M. V., Stepanov, N. A., & Sergeev, V. A. (2019). On the evaluation of data quality in the OMNI interplanetary magnetic field database. *Space Weather*, *17*(3), 476–486. https://doi.org/10.1029/2018SW002113

Webb, D. F., & Howard, T. A. (2012). Coronal mass ejections: Observations. *Living Reviews in Solar Physics*, *9*, 3. https://doi.org/10.12942/lrsp-2012-3